Kondo, A.	G-protein-coupled receptor signaling in yeast				
Hashimoto N, Sasaki R, Nishimura H, Yoshida K, Miyawaki D, Nakayama M, Uehara K, Okamoto Y, Ejima Y, Azumi A, Matsui T, Sugimura K	Long-term outcome and patterns of failure in primary ocular adnexal mucosa-associated lymphoid tissue lymphoma treated with radiotherapy	Int J Radiat Oncol Biol Phys.	82	1509-14	2011
Komatsu S, Fukumoto T, Demizu Y, Miyawaki D, Terashima K, Niwa Y, Mima M, Fujii O, Sasaki R, Yamada I, Hori Y, Hishikawa Y, Abe M, Ku Y, Murakami M	The effectiveness of particle radiotherapy for hepatocellular carcinoma associated with inferior vena cava tumor thrombus	J Gastroenterol	46	913-20	2011
Komatsu S, Fukumoto T, Demizu Y, Miyawaki D, Terashima K, Sasaki R,	Clinical results and risk factors of proton and carbon ion therapy for hepatocellular carcinoma	Cancer	117	4890-904	2011

Hori Y, Hishikawa Y, Ku Y, Murakami M					
Sasaki R, Yasuda K, Abe E, Uchida N, Kawashima M, Uno T, Fujiwara M, Shioyama Y, Kagami Y, Shibamoto Y, Nakata K, Takada Y, Kawabe T, Uehara K, Nibu K, Yamada S	Multi-institutional analysis of solitary extramedullary plasmacytoma of the head and neck treated with curative radiotherapy	Int J Radiat Oncol Biol Phys.	82	626-34	2011
Yoshida K, Sasaki R, Nishimura H, Miyawaki D, Kawabe T, Okamoto Y, Nakabayashi K, Yoshida S, Sugimura K	Radiotherapy for Japanese elderly patients with cervical cancer: preliminary survival outcomes and evaluation of treatment-related toxicity	Arch Gynecol Obstet.	284	1007-14	2011
Ishihara T, Yoden E, Konishi K, Nagase N, Yoshida K, Kurebayashi J, Sonoo H,	Long-term outcome of hypofractionated radiotherapy to the whole breast of Japanese women after breast-conserving surgery	Breast Cancer	22		2012

Murashima N, Sasaki R, Hiratsuka J					
Terashima K, Demizu Y, Hashimoto N, Jin D, Mima M, Fujii O, Niwa Y, Takatori K, Kitajima N, Sirakawa S, Yonson K, Hishikawa Y, Abe M, Sasaki R, Sugimura K, Murakami M	A phase I/II study of gemcitabine-concurrent proton radiotherapy for locally advanced pancreatic cancer without distant metastasis	Radiother Oncol.	103	25-31	2012
Soejima T, Yoden E, NIshimura Y, Ono S, Yoshida A, Fukuda H, Fukuhara N, Sasaki R, Tsujino K, Norihisa Y	Radiation therapy in patients with implanted cardiac pacemakers and implantable cardioverter defibrillators: a prospective survey in Japan	J Radiat Res.	52	516-21	2011
J. Zhang, T. Naka, S. Ohara, K. Kaneko, T. Trevethan, A. Shluger, T. Adschiri	Surface Ligand-Assisted Valence Change in Ceria Nanocrystals	Phys. Rev. B	84	045411-1-9	2011

Z. Tan, H. Abe, S. Ohara	Ordered Deposition of Pd Nanoparticles on Sodium Dodecyl Sulfate-Functionalized Single-Walled Carbon nanotubes	J. Mater. Chem.	21	12008-12014	2011
S. Ohara, Y. Hatakeyama, M. Umetsu, Z. Tan, T. Adschiri	Fabrication of Pd-DNA and Pd-CNT Hybrid Nanostructures for Hydrogen Sensors	Advanced Powder Technology	22	559-565	2011
T. Togashi, S. Takami, K. Kawakami, H. Yamamoto, T. Naka, K. Sato, K. Abe, T. Adschiri,	Continuous Hydrothermal Synthesis of 3,4-Dihydroxyhydrocinnamic Acid-Modified Magnetite Nanoparticles with Stealth-Functionality against Immunological Response	J. Mater. Chem.	22	9041-9045	2012
M. Taguchi, S. Takami, T. Adschiri, T. Nakane, K. Sato, T. Naka	Simple and rapid synthesis of ZrO2 nanoparticles from Zr(OEt)4 and Zr(OH)4 using a hydrothermal method	Cryst. Eng. Comm.	14	2117-2123	2012
M. Taguchi, S. Takami, T. Adschiri, T. Nakane, K. Sato, T. Naka	Synthesis of surface-modified monoclinic ZrO2 nanoparticles using supercritical water	Cryst. Eng. Comm.	14	2132-2138	2012
A. Sahraneshin, S. Takami, D. Hojo,	Synthesis of shape-controlled organic-hybridized	J. Supercrit. Fluids	62	190-196	2012

K. Minami, T. Arita, T. Adschiri	hafnium oxide nanoparticles under sub- and supercritical hydrothermal conditions				
J. Lu, K. Minami, S. Takami, M. Shibata, Y. Kaneko, T. Adschiri	Supercritical Hydrothermal Synthesis and In Situ Organic Modification of Indium Tin Oxide Nanoparticles Using Continuous-Flow Reaction System	ACS Appl. Mater. Interfaces	4	351-354	2012
T. Togashi, M. Umetsu, T. Naka, S. Ohara, Y. Hatakeyama, T. Adschiri	One-pot Hydrothermal Synthesis of an Assembly of Magnetite Nanoneedles on a Scaffold of Cyclic-diphenylalanine Nanorods	Journal of Nanoparticle Research	13	3991-3999	2011
H. Watanabe, K. Kanazaki, T. Nakanishi, H. Shiotsuka, S. Hatakeyama, M. Kaieda T. Imamura, M. Umetsu, I. Kumagai	Biomimetic engineering of modular bispecific antibodies for biomolecule immobilization	Langmuir	27	9656-9661	2011
R. Asano, K. Ikoma, I. Shimomura, S. Taki, T. Nakanishi, M. Umetsu, I. Kumagai	Cytotoxic enhancement of a bispecific diabody by format conversion to tandem single-chain variable fragment (taFv) THE CASE OF THE hEx3 DIABODY	The Journal of Biological Chemistry	286	1812–1818	2011

T. Togashi, N. Yokoo, M. Umetsu, S. Ohara, T. Naka, S. Takami, H. Abe, I. Kumagai, T. Adschiri,	Material-binding peptide application -ZnO crystal structure control by means of a ZnO-binding peptide-	Journal of Bioscience and Bioengineering	111	140-145	2011
S. Watanabe, H. Hyodo, H. Taguchi, K. Soga, Y. Takanashi, M. Matsumoto	Calcination- and Etching-Free Photolithography of Inorganic Phosphor Films Consisting of Rare Earth Ion Doped Nanoparticles on Plastic Sheets	ADVANCED FUNCTIONAL MATERIALS	21	4264-4269	2011
H. Yoshida, K. Morita, B.N. Kim, K. Hiraga, K. Yamanaka, K. Soga T. Yamamoto	Low-Temperature Spark Plasma Sintering of Yttria Ceramics with Ultrafine Grain Size	JOURNAL OF THE AMERICAN CERAMIC SOCIETY	94	3301-3307	2011
M. Kamimura, N. Kanayama, K. Tokuzen, K. Soga Y. Nagasaki	Near-infrared (1550 nm) in vivo bioimaging based on rare-earth doped ceramic nanophosphors modified with PEG-b-poly(4-vinyl benzylphosphonate)	NANOSCALE	3	3705-3713	2011

Journal of Surgical Research **174,** 48–55 (2012)
doi:10.1016/j.jss.2010.11.884

Sentinel Node Mapping with Thermoresponsive Magnetic Nanoparticles in Rats

Kunihiko Hiraiwa, M.D.,* Masakazu Ueda, M.D., Ph.D.,*,[1] Hiroya Takeuchi, M.D., Ph.D.,* Takashi Oyama, M.D.,* Tomoyuki Irino, M.D.,* Takahisa Yoshikawa, M.D.,* Akihiko Kondo, Ph.D.,† and Yuko Kitagawa, M.D., Ph.D.*

**Department of Surgery, Keio University School of Medicine, Shinjuku, Tokyo, Japan; and †Department of Chemical Science and Engineering, Graduate School of Engineering, Kobe University, Nada, Kobe, Japan*

Originally submitted June 4, 2010; accepted for publication November 9, 2010

Background. **In this study, we investigated the ability of magnetic resonance imaging (MRI) after interstitial administration of thermoresponsive magnetic nanoparticles to detect the sentinel lymph node (SLN).**

Materials and Methods. **Postcontrast MRI scans were acquired following subcutaneous injection of thermoresponsive magnetic nanoparticles into the thoracic wall of rats. The signal-to-noise ratio of axillary lymph nodes was calculated to assess whether the SLN could be detected by MRI. In a second experiment, after injecting thermoresponsive magnetic nanoparticles, i.e., Therma-Max 36, Therma-Max 42, Therma-Max 55, and Ferridex, into the subserosa of the cecum of rats, the injection sites, the SLNs, and the distant lymph nodes were resected and examined histologically in order to determine which nanoparticles, if any, were specifically retained in the SLN.**

Results. **MRI showed that the signal-to-noise ratio of axillary SLNs was significantly lower 24 h after injection of Therma-Max 42 than on the precontrast images ($P < 0.05$). Histologic evaluation revealed that Therma-Max 36 aggregated at body temperature and did not migrate to the SLN. Therma-Max 42, on the other hand, aggregated, and the particles became large enough to be retained in the SLNs. Therma-Max 55 and Ferridex did not aggregate, and they both migrated to the SLNs and the distant lymph nodes.**

Conclusions. **The results of this study showed that thermoresponsive magnetic nanoparticles could be targeted to the SLN by adjusting the temperature at which they aggregate, and that they could be used as a contrast agent for SLN mapping by MRI.**

Key Words: **sentinel lymph node; thermoresponsive magnetic nanoparticle; magnet resonance imaging; lymphography.**

INTRODUCTION

Determination whether tumor cells have spread to lymph nodes plays an important role in staging cancer and in designing appropriate treatment protocols. Axillary node metastasis is an important prognostic indicator in breast cancer. The sentinel lymph node (SLN) is defined as the first lymph node to which lymph from the primary tumor drains, and it is therefore at highest risk for regional metastasis *via* lymphatic spread. Surgical biopsy of the SLN is now becoming standard practice for minimally invasive surgery in early stage breast cancer because of the proven accuracy of staging [1–3], and it is useful for planning the operative field and selective lymphadenectomy, and for avoiding unnecessary extended lymphadenectomies. As a result, surgery on the basis of the SLN concept improves the postoperative quality of life of patients.

The lymphoscintigraphic method and blue dye method are currently the most widely used methods of identifying the SLN for biopsy in breast cancer patients [3], but there are some disadvantages and potential pitfalls in SLN mapping by these methods. The scintigraphic method is unavailable in hospitals that do not have a nuclear medicine department, and it has the disadvantages of involving the use of a radioactive tracer and technical difficulties with external γ-probe counting. It also has the disadvantage of poor spatial resolution imaging, which limits its value for

[1] To whom correspondence and reprint requests should be addressed at Department of Surgery, School of Medicine, Keio University, 35 Shinanomachi, Shinjuku-ku, Tokyo, Japan, 160-8582. E-mail: m_ueda@sc.itc.keio.ac.jp.

0022-4804/$36.00

an accurate identification of the detailed anatomy of the draining lymphatic basin. Difficulty in identifying the location of lymph nodes presents an impediment to precise surgery.

The SLN concept also appears to be applicable to gastrointestinal cancers, and SLN detection may contribute to minimally invasive surgery, selective lymphadenectomy, and accurate staging by the lymphoscintigraphic method with intraoperative γ probe counting [4–8]. However, this method cannot be used for preoperative analysis of the accurate anatomic location of the SLN because of its limited spatial resolution [6, 7].

Lymphangiography by computed tomography (CT) has recently been reported to be feasible [9–12], but MRI has a number of potential advantages over lymphoscintigraphy and CT lymphangiography, including higher spatial resolution that enables depiction of lymphatic channels, higher temporal resolution, acquisition of three-dimensional images, and the absence of exposure to ionizing radiation.

Recent studies have shown the potential of magnetic resonance imaging (MRI) after interstitial administration of superparamagnetic iron oxide (SPIO) and ultrasmall superparamagnetic iron oxide (USPIO) in both animals [13–19] and humans [20–22]. However, according to the previous reports on MR lymphography, SPIO and USPIO were not retained in the sentinel lymph node (SLN) and flowed through it to the next nodes in line very soon after the injection. The ideal SLN imaging agent needs to have a particle size small enough to enter the lymphatic vessels, yet large enough to be retained in the SLN.

Newly developed thermoresponsive magnetic nanoparticles (Therma-Max; Magnabeat, Chiba, Japan) undergo a reversible transition between dispersion and aggregation as a function of temperature. The hypothesis that we tested in this study is that these magnetic nanoparticles are small enough to enter the lymphatic vessels, but then aggregate at body temperature and become large enough to be retained in the SLN, and will be useful for SLN mapping by MRI. In this study, we investigated the ability of MRI with thermoresponsive magnetic nanoparticles to detect SLN.

MATERIALS AND METHODS

Contrast Agents

The thermoresponsive property of Therma-Max derives from the N-isopropyl acrylamide coating of magnetic nanoparticles. Therma-Max undergoes a reversible transition between dispersion and aggregation as a function of temperature (Fig. 1). It has a low critical solution temperature of around 34°C and becomes insoluble at higher temperatures. The insoluble N-isopropyl acrylamide causes the magnetic nanoparticles to aggregate, and they are quickly separated from the solution in a magnetic field. The temperature at which they aggregate can be changed by adjusting dose of N-isopropyl acrylamide. The properties of Therma-Max have been described in detail by Kondo *et al.* [23].

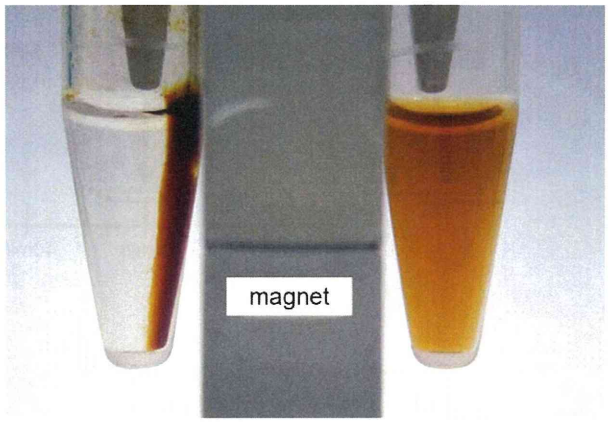

FIG. 1. The heated Therma-Max nanoparticles on the left aggregated and responded to the magnet (A). The cooled Therma-Max nanoparticles on the right did not aggregate and the nanoparticles solution did not respond to the magnet (B). Therma-Max showed a reversible transition between dispersion and aggregation as a function of temperature. (Color version of figure is available online.)

MR Imaging

All MRI examinations were performed with a 4.7-T MR unit (Varian INOVA, Varian Inc., Palo Alto, CA). The MRI protocol started with a T1-weighted gradient-echo localizer sequence composed of three section stacks oriented in the coronal and transverse planes. The MR imaging parameters were as follows: TE/TR 20/2000 ms, field of view (FOV) 10 × 5 cm, slice thickness 1 mm, and number of excitations 4.

Phantom Experiment

The phantom was constructed in a concentric manner from cylindrical plastic bottles containing the following substances from the core to the exterior: water, air. This phantom was scanned at various echo times (TEs) and a fixed repetition time (TR; 180 ms). The particles had a T1 relaxivity of 48.8 $mM^{-1}s^{-1}$ and a T2 relaxitivity of 726.4 $mM^{-1}s^{-1}$ (determined in aqueous solution, 37°C).

Image Interpretation and Data Analysis

The signal intensity of muscle tissue served as an internal standard for calculating the standardized signal intensity of a lymph node according to the following formula: SI = IL/IM, where SI = standardized signal intensity, IL = signal intensity of the lymph node, and IM = signal intensity of the muscle tissue. The reduced signal intensity (SI red) of a lymph node was calculated as follows: SI red (%) = (SI post – SI pre)/(SI pre × 100), where SI pre is the precontrast standardized signal intensity of the lymph node and SI post is the postcontrast standardized signal intensity of the lymph node. Differences between SI pre and SI post were tested for statistical significance by using Wilcoxon's test for paired samples. Differences between the SI of the SLN and that of a distant lymph node were tested by Fischer's exact test. A P value <0.05 was considered to indicate statistical significance.

Animals and Anesthesia

All animal studies were approved by the institutional review board for animal research. The animals used were 6-wk-old Donryu rats weighing 180–200 g. The body temperature of the rats was 38.5 ± 0.4°C. The

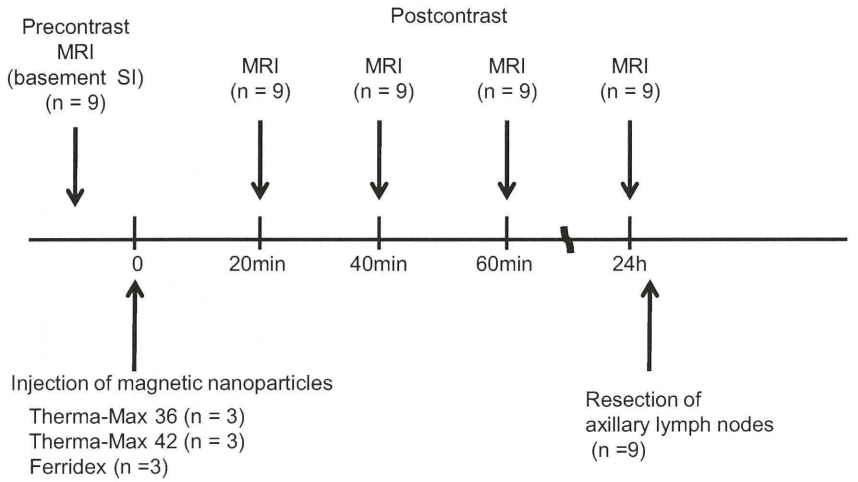

FIG. 2. The scheme of axillary SLN mapping with MRI. A precontrast MRI lymphogram was obtained, and postcontrast MRI lymphograms were obtained 20, 40, 60, min, and 24 h after injection of the magnetic nanoparticles.

injection of magnetic nanoparticles, resection of lymph nodes and injection sites, and histologic evaluation of lymph nodes in the mesentery were conducted with the animals sedated with an intraperitoneal injection of ketamine hydrochloride (50 mg per kilogram body weight ketavet; Parke-Davis, Berlin, Germany). MRI was performed under general anesthesia. All animals were killed by exsanguinations under deep anesthesia.

Axillary SLN Mapping with Magnetic Nanoparticles

Three types of magnetic nanoparticles were assessed; Therma-Max nanoparticles that aggregate at 36°C (Therma-Max 36), Therma-Max nanoparticles that aggregate at 42°C (Therma-Max 42), and magnetic nanoparticles not coated with a thermoresponsive polymer (Ferridex; Eiken Chemical Co., Tokyo, Japan). All of them were diluted with saline and contained 0.6 mg/mL of iron.

The diameter of all nanoparticles as measured by dynamic light scattering was approximately 100 nm, which is a favorable size for entering lymphatic vessels and reaching lymph nodes. A 1.0 mL syringe and a 26 gauge needle were used to subcutaneously inject 0.1 mL of the nanoparticle solution at five points on the right side of the thoracic wall of three rats each. A precontrast MRI lymphogram was obtained, and postcontrast MRI lymphograms were obtained 20, 40, 60 min, and 24 h after injection of the contrast material. Subcutaneous injection of isosulfan blue (lymphazurin; Covidien, Mansfield, MA) into the thoracic wall of the rats was performed to visualize the location of the axillary SLN, and they were resected and histologically examined with Prussian blue. The scheme of axillary SLN mapping with MRI was shown in Figure 2.

Intestinal SLN Mapping with Magnetic Nanoparticles

Injection of lymphazurin into the subserosa of cecum of rats was performed to visualize the location of the SLN and distant lymph nodes in the mesentery (Fig. 3). Three types of magnetic nanoparticles were assessed; Therma-Max 36, Therma-Max 42, and Therma-Max nanoparticles that aggregate at 55°C (Therma-Max 55). A 1.0 mL syringe and a 26 gauge needle were used to inject 0.04 mL of the nanoparticles solution at five points in the subserosal layer of the cecum of ten rats each. The SLN and the distant lymph nodes were resected at 5 min, 1, 4, 8, 12, and 24 h, and 2, 3, 5, and 7 d after the injection and examined histologically. All excised LNs and the injection sites were histologically evaluated after staining with Prussian blue. The scheme of intestinal SLN mapping with magnetic nanoparticles was shown in Figure 4.

RESULTS

Axillary SLN Mapping with Magnetic Nanoparticles

Isosulufan blue injection after MRI confirmed the location of the SLN. The location and the size of the SLNs at necropsy were consistent with the MRI findings. The postcontrast MRI findings following subcutaneous injection of Therma-Max 36 showed no marked changes in the SI of the axillary SLN. Histologic evaluation showed no influx of magnetic nanoparticles into the SLN. Postcontrast MRI following subcutaneous injection of Therma-Max 42 showed reduced SI of the axillary SLN (Fig. 5A and B). Histologic evaluation of the axillary SLN showed no magnetic nanoparticles before the injection and the presence of magnetic nanoparticles after the injection (Fig. 5C and D). Postcontrast MRI following subcutaneous injection of Ferridex showed reduced SI of the axillary SLN. Histologic

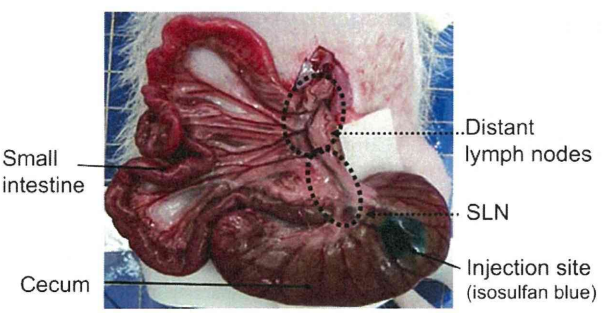

FIG. 3. Mesentery lymph nodes in rats. Injection of isosulfan blue into the subserosa of cecum visualized the location of SLNs and distant lymph nodes. (Color version of figure is available online.)

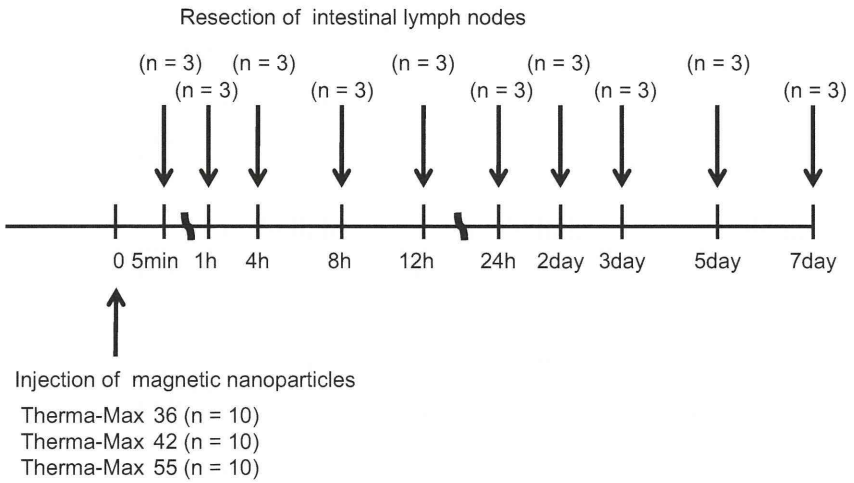

FIG. 4. The scheme of intestinal SLN mapping with magnetic nanoparticles. The SLN and the distant lymph nodes were resected at 5 min, 1, 4, 8, 12, and 24 h, and 2, 3, 5, and 7 d after the injection and examined histologically.

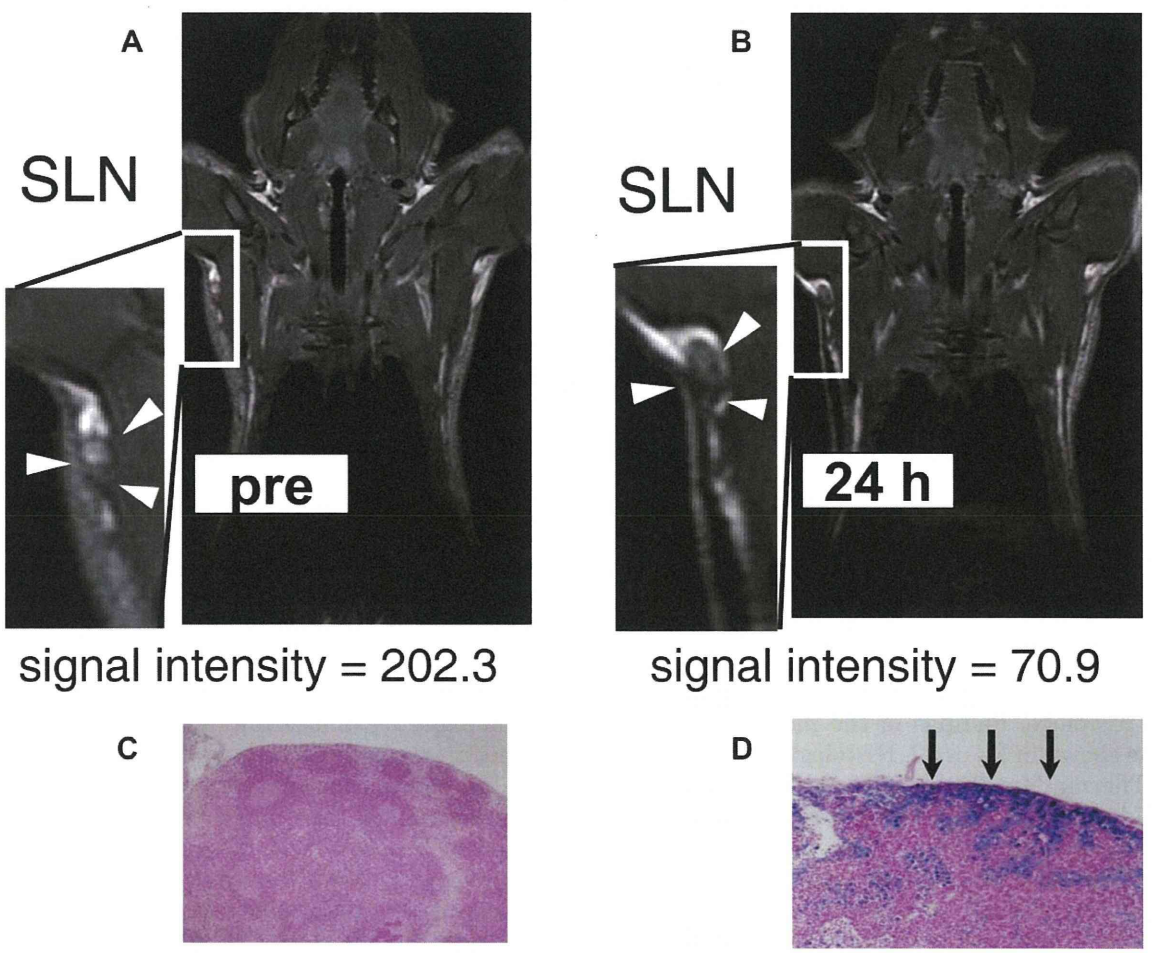

FIG. 5. Pre- and postcontrast MRI following subdermal injection of Therma-Max 42. (A) Precontrast MRI showed the axillary lymph node (arrowheads) with baseline signal intensity. (B) Postcontrast MRI (24 h after injection) showed reduced signal intensity of the axillary SLN (arrowheads). (C) Histologic evaluation of precontrast SLN. (D) Histologic evaluation of postcontrast SLN revealed influx of magnetic nanoparticles (arrows). (Color version of figure is available online.)

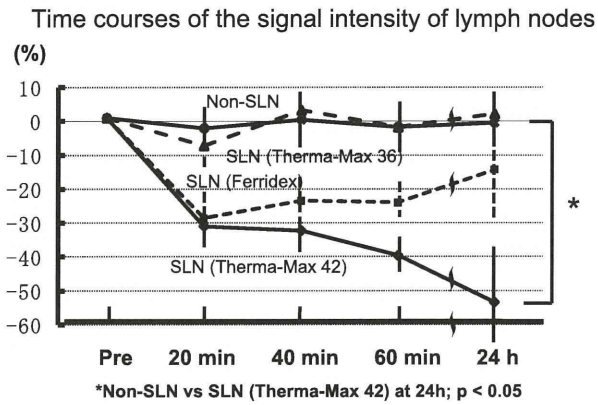

FIG. 6. The time courses of signal intensity (SI) of the SLN and distant LN. SI of either SLN with Therma-Max 36 or non-SLN was not changed. The minimum SI of the SLN with Ferridex occurred 20 min after the injection. The minimum SI of the SLN with Therma-Max 42 occurred 24 h after the injection. Twenty-four hours after the injection, the SI of SLN with Therma-Max 42 was significantly lower than that of non-SLN ($P < 0.05$). Therma-Max 42 made more remarkable changes of SI than Ferridex.

evaluation of the axillary SLN showed the presence of Ferridex nanoparticles.

The time courses of SI of the SLN and the non-SLN are shown in Figure 6. The non-SLN is an ipsilateral axillary lymph node. SI of the SLN and non-SLN was unchanged by Therma-Max 36. It aggregated at the site of injection as a result of exposure to body temperature, and did not migrate to the SLN. Ferridex entered lymphatic vessels, and the minimum SI of the SLN occurred 20 min after the injection, after which the SI of the SLN gradually increased. Therma-Max 42 entered lymphatic vessels, and the minimum SI of the SLN occurred 24 h after the injection. At 24 h after the injection, the SI of SLN was significantly lower than that of the non-SLN ($P < 0.05$). The changes in SI observed when Therma-Max was used as a contrast agent were greater than with Ferridex.

Intestinal SLN Mapping with Magnetic Nanoparticles

The summary of histological evaluation of the mesentery lymph nodes were shown in Table 1. The representatives of histologic findings of the mesentery lymph nodes were shown in Figure 7. Histologic evaluation revealed of Therma-Max 36 particles only at the injection site (Fig. 7A and B), suggesting that they aggregated in response to body temperature and did not migrate to the SLN. This result is consistent with the results of histological evaluation of axillary lymph nodes. Therma-Max 42 particles were found both at the injection site and in the SLN (Fig. 7C), but not in the distant lymph nodes (Fig. 7D). Therma-Max 55 and Ferridex particles were found at the injection site, in the SLN (Fig. 7E and G), and in the distant lymph nodes (Fig. 7F and H).

TABLE 1

Detection of Magnetic Nanoparticles in the Lymph Nodes

	Therma-Max 36		Therma-Max 42		Therma-Max 55		Ferridex	
Time	SLN	DLN	SLN	DLN	SLN	DLN	SLN	DLN
5 min	–	–	–	–	+	–	+	–
1 h	–	–	+	–	+	–	+	–
4 h	–	–	+	–	+	–	+	–
8 h	–	–	+	–	+	–	+	+
12 h	–	–	+	–	+	–	+	+
24 h	–	–	+	–	+	+	+	+
2 d	–	–	+	–	+	+	+	–
3 d	–	–	+	–	+	+	+	–
5 d	–	–	+	–	+	+	+	–
7 d	–	–	+	–	+	+	+	–

SLN = sentinel lymph node; DLN = distant lymph node.
+, detected; -, not detected.

DISCUSSION

Lymphatic mapping and SLN biopsy is one of the most interesting recent developments in surgical oncology. This approach allows patients to be treated in an early stage without unnecessary regional lymph node dissection. The SLN is the lymph node that receives direct drainage from the primary lesion [24]. Second-tier and third-tier nodes receive drainage in a later phase.

The lymphoscintigraphic method and blue dye method are currently the most widely used methods of identifying the SLN for biopsy in cancer patients [3]. However, these methods cannot be used for preoperative analysis of the accurate anatomical location of the SLN because of its limited spatial resolution [6, 7]. MR lymphography with magnetic nanoparticles will enable us to predict the accurate anatomic location of the SLN preoperatively. It has a number of potential advantages over lymphoscintigraphy, including higher spatial resolution that enables depiction of lymphatic channels, higher temporal resolution, acquisition of three-dimensional images, and the absence of exposure to ionizing radiation.

Although recent studies have shown the potential of MRI after interstitial administration of SPIO and USPIO as a means of identifying the SLN, they were not retained in the SLN and flowed through to the next node in line very soon after injection. The same as radiocolloids and blue dye, spill-over of magnetic nanoparticles from the SLN to distant lymph nodes may increase the labeling of non-SLNs. The interstitial MR lymphography with thermoresponsive magnetic nanoparticles adequately identified the axillary SLN.

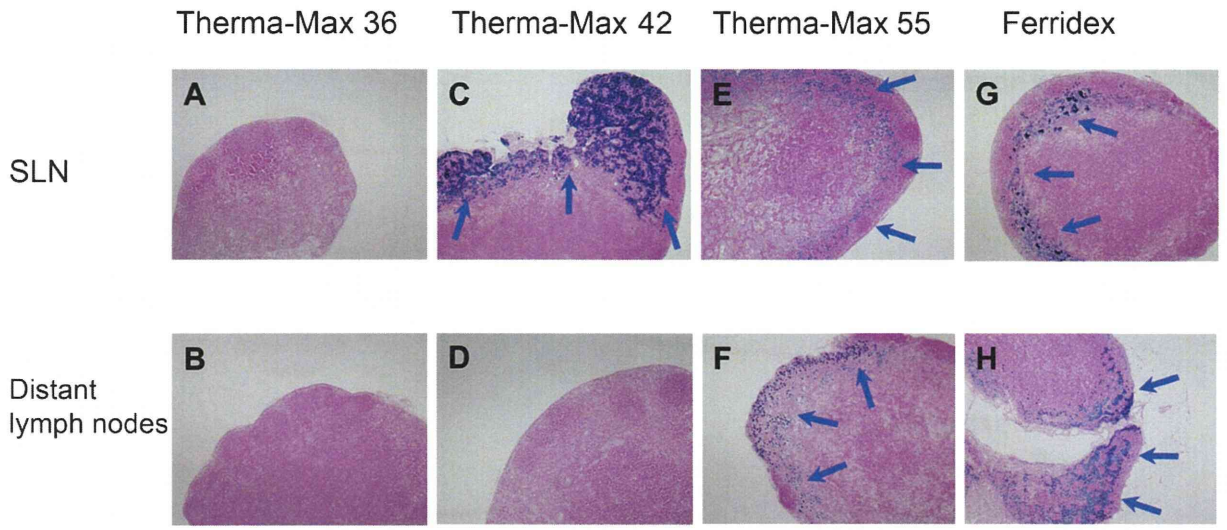

FIG. 7. The histologic evaluation of mesentery lymph nodes in rats. (A) SLN with Therma-Max 36 showed no magnetic nanoparticles. (B) Distant lymph nodes with Therma-Max 36 showed no magnetic nanoparticles. (C) SLN with Therma-Max 42 showed influx of magnetic nanoparticles (arrows). (D) Distant lymph nodes with Therma-Max 42 showed no magnetic nanoparticles. (E) SLN with Therma-Max 55 showed influx of magnetic nanoparticles (arrows). (F) Distant lymph nodes with Therma-Max 55 showed influx of magnetic nanoparticles (arrows). (G) SLN with Ferridex showed influx of magnetic nanoparticles (arrows). (H) Distant lymph nodes with Ferridex showed influx of magnetic nanoparticles (arrows). (Color version of figure is available online.)

Magnetic nanoparticles in the SLN can be detected with the newly developed superconducting quantum interference devices (SQUIDs) such as the SentiMag (Endomagnetics Ltd., London, U.K.). However, the SQUIDs require a large space and equipment. They are not useful when the SLN is located deep inside the body. MRI, on the other hand, has already been used clinically worldwide and is especially useful when the SLN is located deep inside the body. MRI is useful for preoperative SLN mapping with thermoresponsive magnetic nanoparticles and SQUIDs might be useful for intraoperative SLN mapping with thermoresponsive magnetic nanoparticles.

The intestinal SLN mapping in this study revealed that thermoresponsive magnetic nanoparticles could be specifically targeted to the SLN by adjusting the temperature at which they aggregate (Fig. 8). Therma-Max 42 entered lymphatic vessels and the minimum SI of the SLN occurred at 24 h after the injection, suggesting that Therma-Max 42 had been retained in the SLN. Ferridex entered the lymphatic vessels, and the minimum SI of the SLN occurred 20 min after the injection, and then gradually increased, suggesting that Ferridex may pass through the SLN rapidly. Ferridex and Therma-Max 55 sometimes reached the distant lymph nodes. Therma-Max 42 resulted in more marked changes in SI as a contrast agent than Ferridex did, suggesting that Therma-Max may be a more sensitive tracer for MR lymphography. The changes in SI with Therma-Max were slower than with Ferridex. These findings suggest that clinical use of Therma-Max might be feasible, for example, for endoscopic injection to detect gastrointestinal SLNs.

Differentiation of the SLN from distant lymph nodes and lymph nodes draining other anatomical sites is critical to SLN biopsy because examining the true SLN for extensive histologic evaluation increases the accuracy of staging. Although Therma-Max does not have specific lymphotropic properties, it is likely that it drains from the interstitial space into lymphatic pathways through thin-walled fenestrated lymphatic microvessels, similar to other extracellular, water-soluble, low-molecular solutes. The locations and the sizes of the SLNs resected from the animals at necropsy *post mortem* in our animals appeared to be consistent with the MR lymphography findings. Although these are preliminary results obtained in tumor-free animals, this method may have potential as a means of SLN mapping that will enable more precise and minimally invasive SLN biopsy.

Evaluation for toxicities of magnetic nanoparticles is mandatory. Unfortunately, no data about toxicities of magnetic nanoparticles in human being has been obtained. At least no side effects, including allergic reactions, were recognized in rats in this study. We plan to validate the SLN mapping with MRI using Therma-Max and to evaluate toxicities in larger animals.

In conclusion, MR lymphography with Therma-Max enables visualization of SLN. This method will reduce the labeling of non-SLNs seen in previous reports on interstitial MR lymphography. Although further study is required to evaluate its clinical efficacy in other animals and in humans, and to compare it with

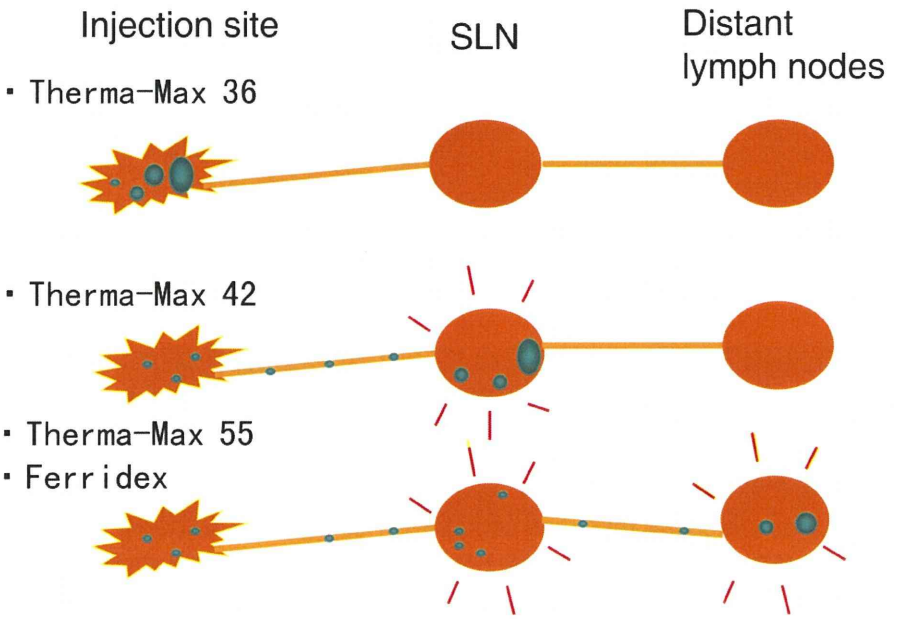

FIG. 8. Schema of each nanoparticle to identify the SLN. Therma-Max 36 aggregated at the site of injection according to body temperature and did not migrate to the SLN. Therma-Max 42 entered lymphatic vessels. It gradually aggregated according to body temperature and became large enough to be retained in the SLNs. Therma-Max 55 and Ferridex did not aggregate according to body temperature in rats. It also migrated to distant LNs. (Color version of figure is available online.)

scintigraphic and blue-dye methods, it may be an ideal method for achieving minimally invasive surgery in early stage cancers.

ACKNOWLEDGMENTS

The authors acknowledge support for this work by JSPS KAKENHI 20790938.

REFERENCES

1. Veronesi U, Galimberti V, Zurrida S, et al. Sentinel lymph node biopsy as an indicator for axillary dissection in early breast cancer. Eur J Cancer 2001;37:454.
2. Schrenk P, Shamiyeh A, Wayand W. Sentinel lymph-node biopsy compared to axillary lymph-node dissection for axillary staging in breast cancer patients. Eur J Surg Oncol 2001;27:378.
3. Krag D. Minimal invasive staging for breast cancer: Clinical experience with sentinel lymph node biopsy. Semin Oncol 2001; 28:229.
4. Kitagawa Y, Fujii H, Mukai M, et al. The role of the sentinel lymph node in gastrointestinal cancer. Surg Clin North Am 2000;80:1799.
5. Takeuchi H, Fujii H, Ando N, et al. Validation study of radio-guided sentinel lymph node navigation in esophageal cancer. Ann Surg 2009;249:757.
6. Kitagawa Y, Fujii H, Mukai M, et al. Radio-guided sentinel node detection for gastric cancer. Br J Surg 2002;89:604.
7. Kitagawa Y, Kitajima M. Gastrointestinal cancer and sentinel node navigation surgery. J Surg Oncol 2002;79:188.
8. Kitagawa Y, Ohgami M, Fujii H, et al. Laparoscopic detection of sentinel lymph nodes in gastrointestinal cancer: A novel and minimally invasive approach. Ann Surg Oncol 2001;8:86S.
9. Suga K, Yamamoto S, Tangoku A, et al. Breast sentinel lymph node navigation with three-dimensional interstitial multidetector-row computed tomographic lymphography. Invest Radiol 2005;40:336.
10. Suga K, Ogasawara N, Okada M, et al. Interstitial CT lymphography-guided localization of breast sentinel lymph node: Preliminary results. Surgery 2003;133:170.
11. Suga K, Yuan Y, Okada M, et al. Breast sentinel lymph node mapping at CT lymphography with iopamidol: Preliminary experience. Radiology 2004;230:543.
12. Hayashi H, Tangoku A, Suga K, et al. CT lymphography-navigated sentinel lymph node biopsy in patients with superficial esophageal cancer. Surgery 2006;139:224.
13. Hamm B, Taupitz M, Hussmann P, et al. MR lymphography with iron oxide particles: Dose-response studies and pulse sequence optimization in rabbits. AJR Am J Roentgenol 1992; 158:183.
14. Tanoura T, Bernas M, Darkazanli A, et al. MR lymphography with iron oxide compound AMI-227: Studies in ferrets with filariasis. AJR Am J Roentgenol 1992;159:875.
15. Weissleder R, Elizondo G, Josephson L, et al. Experimental lymph node metastases: Enhanced detection with MR lymphography. Radiology 1989;171:835.
16. Vassallo P, Matei C, Heston WD, et al. Characterization of reactive versus tumor-bearing lymph nodes with interstitial magnetic resonance lymphography in an animal model. Invest Radiol 1995;30:706.
17. Rogers JM, Jung CW, Lewis J, et al. Use of USPIO-induced magnetic susceptibility artifacts to identify sentinel lymph nodes and lymphatic drainage patterns. I. Dependence of artifact size with subcutaneous Combidex dose in rats. Magn Reson Imaging 1998;16:917.
18. Taupitz M, Wagner S, Hamm B, et al. Interstitial MR lymphography with iron oxide particles: Results in tumor-free and VX2 tumor-bearing rabbits. AJR Am J Roentgenol 1993;161:193.
19. Torchia MG, Nason R, Danzinger R, et al. Interstitial MR lymphangiography for the detection of sentinel lymph nodes. J Surg Oncol 2001;78:151. discussion 157.
20. McCauley TR, Rifkin MD, Ledet CA. Pelvic lymph node visualization with MR imaging using local administration of

ultra-small superparamagnetic iron oxide contrast. J Magn Reson Imaging 2002;15:492.
21. Imano H, Motoyama S, Saito R, et al. Superior mediastinal and neck lymphatic mapping in mid- and lower-thoracic esophageal cancer as defined by ferumoxides-enhanced magnetic resonance imaging. Jpn J Thorac Cardiovasc Surg 2004;52:445.
22. Ishiyama K, Motoyama S, Tomura N, et al. Visualization of lymphatic basin from the tumor using magnetic resonance lymphography with superparamagnetic iron oxide in patients with thoracic esophageal cancer. J Comput Assist Tomogr 2006; 30:270.
23. Kondo A, Kamura H, Higashitani K. Development and application of thermosensitive magnetic immunomicrospheres for antibody purification. Appl Microbiol Biotechnol 1994;41:99.
24. Nieweg OE, Tanis PJ, Kroon BB. The definition of a sentinel node. Ann Surg Oncol 2001;8:538.

ARTICLE

BIOTECHNOLOGY and BIOENGINEERING

The N-Terminal Replacement of an Olfactory Receptor for the Development of a Yeast-based Biomimetic Odor Sensor

Yosuke Fukutani,[1] Tomoko Nakamura,[1] Maiko Yorozu,[1] Jun Ishii,[2] Akihiko Kondo,[3] Masafumi Yohda[1]

[1]Department of Biotechnology and Life Science, Tokyo University of Agriculture and Technology, 2-24-16 Naka-cho, Koganei, Tokyo 184-8588, Japan; telephone: 042-388-7479; fax: 042-388-7479; e-mail: yohda@cc.tuat.ac.jp

[2]Organization of Advanced Science and Technology, Kobe University, Japan

[3]Department of Chemical Science and Engineering, Graduate School of Engineering, Kobe University, Japan

Received 3 July 2011; revision received 26 August 2011; accepted 30 August 2011

Published online 13 September 2011 in Wiley Online Library (wileyonlinelibrary.com). DOI 10.1002/bit.23327

ABSTRACT: For the development of a biomimetic odor-sensing system, we investigated the effects of replacing the N-terminus of an olfactory receptor (OR) on its functional expression in the budding yeast, *Saccharomyces cerevisiae*. Using the mouse olfactory receptor OR226 (mOR226), three types of chimeric ORs were constructed by replacing N-terminal regions of mOR226 with the corresponding regions of the rat I7 receptor, which is known to be functionally expressed in yeast. The replacement of the N-terminal region of mOR226 dramatically affected the expression and localization of the receptor and improved the sensing ability of the yeast cells for the odorant. Furthermore, the replacement of the endogenous yeast G-protein α subunit (Gpa1) by the OR-specific G_{olf} drastically elevated the odorant-sensing ability of the yeast cells and caused the cells to display a dose-dependent responsiveness to the odorant. Because of the suitability of yeast cells for screening large-scale libraries, the strategy presented here would be useful for the establishment of advanced biomimetic odor-sensing systems.

Biotechnol. Bioeng. 2012;109: 205–212.

KEYWORDS: olfactory receptor; GPCR; *Saccharomyces cerevisiae*; biosensing

Introduction

Despite the development of recent chemical-sensing systems, these methods cannot compete with the capabilities of the animal olfactory system. Thus, biomimetic systems have attracted much attention for detecting odorous substances. These systems are expected to enable the quantification of flavors or fragrances and/or the avoidance of harmful agents or explosive accidents (Marrakchi et al., 2007). Such systems would be powerful tools not only for industrial applications but also for understanding the functions of olfactory receptors (ORs) and the unknown functions of the olfactory system.

Animals can sense and distinguish a variety of odorants using olfactory cells equipped with OR that are located on the cell membranes and bind to specific chemical compounds (Buck and Axel, 1991). While only one OR is expressed in an olfactory neuron cell, each OR exhibits flexibility in its binding specificity for odor ligands (Malnic et al., 1999). The olfactory system is likely to determine the identity of a particular odorant by integrating the responses of various olfactory cells (Bargmann, 2006; Chess et al., 1994; Serizawa et al., 2003). The number of functional OR genes is quite different among organisms. While putative OR genes occupy approximately 3% of the mammalian genome (Niimura and Nei, 2005), not all of them are expressed to produce functional ORs (Buck and Axel, 1991). Approximately 350 functional OR genes, which compose nearly one-third of the G-protein-coupled receptor (GPCR) family, have been identified in humans (Niimura and Nei, 2005). The ORs of rodents are often used as models for studying the olfactory system (Nei et al., 2008; Zhang and Firestein, 2002). Reflecting their sophisticated olfactory system, mice and rats have more than 1,400 putative OR genes, and nearly three-fourths of these have been shown to be functional (Nei et al., 2008; Zhang and Firestein, 2002). ORs are members of the GPCR family, consisting of the

Correspondence to: Masafumi Yohda

Contract grant sponsor: Secom Science and Technology Foundation

Additional Supporting Information may be found in the online version of this article.

largest group of integral membrane proteins, which share a seven-transmembrane protein structure (Buck and Axel, 1991). The specific binding of an odor ligand to an OR transmits a signal inside the cells through the intracellular peripheral membrane heterotrimeric guanine nucleotide-binding proteins (G-proteins; consisting of the Gα-, Gβ- and Gγ-subunits).

The eukaryotic, unicellular yeast *Saccharomyces cerevisiae* offers significant advantages for studying heterologous GPCRs. Because of their uncompetitive and monopolistic G-protein signaling pathway, yeast can be used to simplify the complicated signaling pathways of higher eukaryotic cells (Iguchi et al., 2010; Togawa et al., 2010). Because yeast are known to be able to functionally express a wide range of GPCRs derived from mammals, such as the somatostatin receptors, P2Y12 purinergic receptor, and β2 adrenergic receptor (Iguchi et al., 2010; O'Malley et al., 2009; Pausch et al., 2004), their use as biosensors for detecting signals from heterologous GPCRs would be logical. Moreover, because of rapid cell growth and ease of genetic modifications, yeast is suitable host cells for screening large-scale libraries (Ishii et al., 2010). Therefore, the functional expression of various ORs in yeast cells may promote the understanding of the elusive olfactory system by allowing for comprehensive screenings to uncover the mostly unidentified ligands of the ORs. In addition, mutagenesis approaches can be implemented to obtain OR structural information. Additionally, because yeast can be stored on agar plates or in a dry form, establishing a biomimetic odor sensor using a user-friendly format, such as a cell array (Fukuda et al., 2006) that contains a library of yeast cells expressing various ORs, could be accomplished in the future.

Compared with other GPCRs, expressing the ORs in heterogeneous cells is generally difficult (Fukuda et al., 2004). The human embryonic kidney 293 cell line has mainly been used for OR expression (Katada et al., 2003; Saito et al., 2004). To date, only two reports have demonstrated the functional expression of ORs in yeast. Minic et al. reported that the rat OR I7 (RI7) or human OR17-40 could be functionally expressed in *S. cerevisiae* (Minic et al., 2005a), and Radhika et al. used *S. cerevisiae* to screen for the rat OR226 gene that possesses sensitivity for 2,4-dinitrotoluene (DNT), a mimic for the explosive trinitrotoluene (Radhika et al., 2007). This screen was accomplished by constructing a chimeric OR receptor that had both the N- and C-terminal regions of the endogenous protein replaced with the RI7 receptor. However, only a fraction of the ORs can be functionally expressed in yeast. Therefore, developing a methodology for the efficient functional expression of ORs in yeast is essential for the development of a yeast-based biomimetic odor-sensing system. For this purpose, understanding the functional expression of ORs is of great importance. The N-terminal region of a GPCR is often responsible for several important functions, including expression, membrane localization, and ligand binding (Hatt et al., 1999; Krautwurst et al., 1998). Therefore, investigating how the design of the N-terminus of a chimeric receptor affects the functional expression of the resulting OR is instrumental for developing a yeast-based odor-sensing system.

In this study, we constructed three types of chimeric receptors to investigate the effects of replacing the N-terminal region of the OR on the expression and function of the murine OR226 (mOR226) in yeast cells. All of the chimeric receptors contained a C-terminal substitution of the final 27 aa residues of mOR226 with the corresponding 33 aa residues of RI7 (named N_{intact}OR226). To study the effects of altering the N-terminus of the OR, we also replaced the first 36 or 62 N-terminal aa residues of mOR226 with the equivalent regions of the RI7 receptor (N-terminal 32 or 58 aa residues of RI7; named $cI7_{N32}$OR226 or $cI7_{N58}$OR226, respectively). These substitutions affected the regions of the mOR226 protein from the extracellular N-terminus to the intracellular loop 1 (ICL1) in $cI7_{N32}$OR226 or from the extracellular N-terminus to transmembrane bundle 2 (TM2) in $cI7_{N58}$OR226 (Fig. 1). To examine the sensing abilities of the chimeras for DNT, we selected the firefly luciferase (*luc*) gene as a reporter due to its high sensitivity. Furthermore, we also tested whether the replacement of the endogenous yeast G-protein α-subunit (Gpa1) by the OR-specific $G\alpha_{olf}$ could improve DNT-dependent signaling by enhancing the coupling of the G-protein with the chimeric OR in the yeast cells.

Materials and Methods

Strains and Media

All recombinant DNA manipulations were performed using DH5α *Escherichia coli* (Invitrogen Life Technologies Corp., Carlsbad, CA). *E. coli* transformants were grown in Luria-Bertani media (10 g/L tryptone, 5 g/L yeast extract, and 5 g/L NaCl) supplemented with 100 μg/mL ampicillin.

The *S. cerevisiae* BY4741 strain (Brachmann et al., 1998) and its derivatives were used in this study and are listed in Table I. YPD media contained 10 g/L yeast extract, 20 g/L peptone, and 20 g/L glucose. Synthetic dextrose (SD) media containing 6.7 g/L yeast nitrogen base without amino acids (YNB; BD-Diagnostic Systems, Sparks, MD) and 20 g/L glucose, synthetic lactate (SL) media containing 6.7 g/L YNB and 30 g/L lactate, and synthetic galactose/raffinose (SGR) media containing 6.7 g/L YNB, 20 g/L galactose, and 10 g/L raffinose were supplemented with the appropriate amino acids and nucleotides depending on the desired selectable markers (20 mg/L methionine, 20 mg/L histidine, 60 mg/L leucine, or 20 mg/L uracil). Agar (2% w/v) was added to produce solid media when appropriate.

Plasmid Constructions and Yeast Transformation

The plasmids used in this study are listed in Table I. Three types of chimeric ORs were constructed. The first chimera,

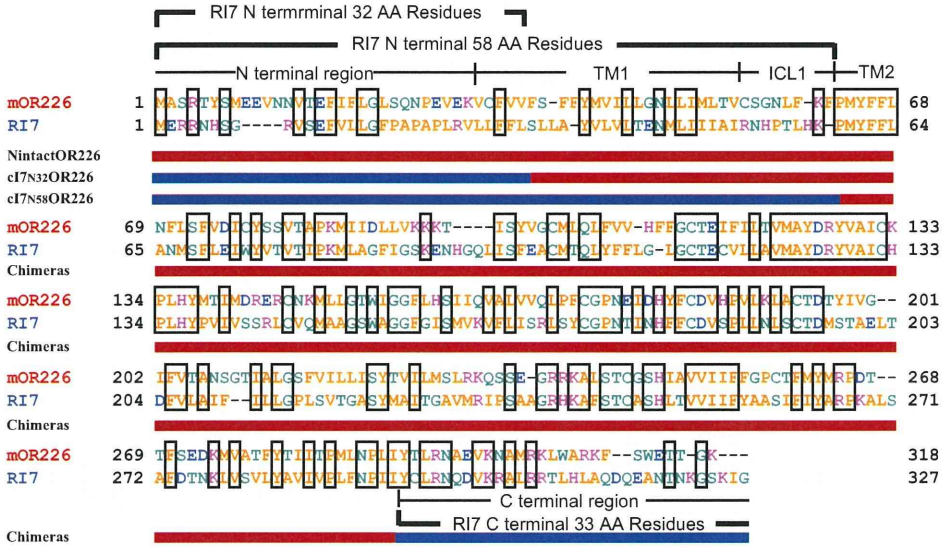

Figure 1. Amino acid sequence alignment of RI7 and mOR226, and design of chimera receptors. transmembrane bundle: TM, intracellular loop: ICL. Red or blue bar indicate that each chimeric ORs have the amino acid sequence from mOR226 or RI7, respectively.

called $N_{intact}OR226$, encoded the mOR226 gene with the last C-terminal 27 aa replaced by the corresponding 33 aa residues of the RI7 receptor, and it was synthesized by DNA2.0 (Medibic Corp., Tokyo, Japan). The synthesized DNA fragment lacked a start codon, and the restriction endonuclease sites for *Xho*I and *Hind*III were attached to both ends. The gene was inserted into the pESC-URA expression vector (Agilent Technologies, Santa Clara, CA) using multiple cloning site 2 (MCS2). The chimeric mOR226 was translated with an N-terminal c-myc tag of the vector. The resulting plasmid was designated as pESCu-myc-OR226. To replace the N-terminal 36 or 62 aa of the $N_{intact}OR226$ gene with the parallel and isometric regions of RI7, the DNA fragments corresponding to the N-terminal RI7/mOR226 fusion (2-32/37-62 aa) or the N-terminal of RI7 (2–58 aa) were synthesized and placed into the *Xho*I and *Bbe*I sites within pESCu-myc-OR226 to produce pESCu-myc-cI7N_{32}OR226 or pESCu-myc-cI7N_{58}OR226, respectively.

For the *luc* reporter assay, the firefly *luc* gene was amplified by PCR from the pGEX-Luc vector (given by Dr. R. Iizuka, Tokyo University) with the primers 5′-gaagatc-taaatggaagacgccaaaaac-3′ and 5′-cccaagcttattacaatagctaa-gaatttcgtcatcgc-3′. The amplified PCR fragment was then inserted into the *Bgl*II and *Hind*III sites of the pMHRS-EGFP plasmid (Ishii et al. unpublished plasmid; EGFP reporter plasmid controlled by FUS1 promoter, which contains 2m origin and HIS3 marker) to replace the *EGFP* gene with the *luc* gene. The generated plasmid was named pMHRS-fLuc.

For G_{olf} expression, the G_{olf} gene was amplified by PCR from the pME18S-Golf vector (given by Prof. K. Tohara, Tokyo University) with the primers 5′-acgcgtcgacatggggtgtt-tgggcaacagcagc-3′ and 5′-gagatcttcacaagagttcgtactgcttgagatgc-3′ and inserted into the *Sal*I and *Bgl*II sites of the pGK425 plasmid (Ishii et al., 2009). The generated plasmid was named pGK-Golf.

Transformation of the *S. cerevisiae* strains was performed using the lithium acetate method (Schiestl et al., 1993). The transformants used in this study are listed and named in Table I. The chimeric receptor expression plasmids (pESCu-myc-cI7$_{N58}$OR226, pESCu-myc-cI7$_{N32}$OR226, or pESCu-myc-OR226) and the *luc* reporter gene expression plasmid (pMHRS-fLuc) were used to transform the IM-50 (*sst2*Δ *ste2*Δ) strain (Ishii et al., 2008). The chimeric receptor expression plasmid (pESCu-myc-cI7$_{N58}$OR226), *luc* reporter gene expression plasmid (pMHRS-fLuc) and Gα_{olf} expression plasmid (pGK-Golf) were also used to transform the MI-150 (*gpa1*Δ *sst2*Δ *ste2*Δ) strain (Iguchi et al., 2010). Transformants were selected on solid SD media containing synthetic drop-out mixtures (Bio 101, Inc., Vista, CA). The presence of the plasmids in the transformants was verified by PCR.

Conditions of Cultivation and Galactose Induction

The induction of chimeric receptor expression was performed as previously described with a slight modification in the temperature (Price et al., 1995). Briefly, colonies were inoculated in SD media and cultured at 30°C until exponential growth was reached (Optical density at 600 nm (D_{600}) was in the range of 1–2). The cells were then washed to remove glucose, cultured for 4–6 h in SL media, pelleted and diluted to an D_{600} of 0.5 in SGR media. Finally, the cells were cultured in SGR media at 30°C for approximately 18 h and harvested within the exponential

Table I. Yeast strains and plasmids used in this study.

Plasmid or strain	Description	Reference or source
Plasmids		
pESC-URA	*URA3*, *GAL10/GAL1* divergent promoters	Agilent Technologies
pESCu-myc-OR226	*URA3*, expression of *myc-N_{intact}OR226* gene by *GAL1* promoter on pESC-URA	This study
pESCu-myc-cI7$_{N32}$OR226	*URA3*, expression of *myc-cI7$_{N32}$OR226* gene by *GAL1* promoter on pESC-URA	This study
pESCu-myc-cI7$_{N58}$OR226	*URA3*, expression of *myc-cI7$_{N58}$OR226* gene by *GAL1* promoter on pESC-URA	This study
pMHRS-fLuc	*HIS3*, expression of *firefly luciferase* (*luc*) gene by *FUS1* promoter	This study
pGK425	*LEU2*, *PGK1* promoter	Ishii et al. (2009)
pGK-Golf	*LEU2*, expression of G_{olf} gene by *PGK1* promoter on pGK425	This study
Strains		
BY4741	*MAT* **a** *his3*Δ1 *leu2*Δ0 met15Δ0 ura3Δ0	Brachmann et al. (1998)
IM-50	BY4741 *sst2*Δ::*AUR1-C ste2*Δ::*LEU2*	Ishii et al. (2008)
MI-150	BY4741 *gpa1*Δ::*kanMX4 sst2*Δ *ste2*Δ	Iguchi et al. (2010)
FL50-N_{intact}OR226	IM-50 harboring pESCu-myc-OR226 and pMHRS-fLuc	This study
FL50-cI7$_{N32}$OR226	IM-50 harboring pESCu-myc-cI7$_{N32}$OR226 and pMHRS-fLuc	This study
FL50-cI7$_{N58}$OR226	IM-50 harboring pESCu-myc-cI7$_{N58}$OR226 and pMHRS-fLuc	This study
FL50-ΔOR	IM-50 harboring pESC-URA and pMHRS-fLuc	This study
FL150-cI7$_{N58}$OR226-Golf	MI-150 harboring pESCu-myc-cI7$_{N58}$OR226, pGK-Golf and pMHRS-fLuc	This study
FL150-ΔOR-Golf	MI-150 harboring pESC-URA, pGK-Golf and pMHRS-fLuc	This study

growth phase (D_{600} was in the range 1–3) (Minic et al., 2005a).

RNA Extraction and Reverse Transcription PCR (RT-PCR)

Total RNA was extracted from yeast cells using the MagExtractor RNA kit (Toyobo Co., Ltd., Osaka, Japan). To remove contaminating DNA, the extracted total RNA was treated with DNase I. The total RNA (100 ng) was reverse transcribed using the PrimeScript RT-PCR kit (Takara Bio Inc., Shiga, Japan) with an oligo dT primer. The partial cDNA of each OR was amplified by PCR with the following primers: 5′-tcctgccccactgcgagtactactat-3′ and 5′-gcgacgtagcgctcttttgacat-3′. The absence of DNA was verified by PCR (non-reverse transcribed) using DNase-treated extracts with the same primers. The generated products were separated by electrophoresis on a 1% agarose gel.

Yeast Protein Extraction

For the extraction of yeast proteins, cells were washed twice with ice-cold water, harvested by centrifugation, and resuspended in an equal volume of ice-cold lysis buffer [50 mM Tris (hydroxymethyl) aminomethane hydrochloride (Tris-HCl; pH 6.8), 1 mM ethylene diamine tetraacetic acid (EDTA), 0.1 mM phenylmethylsulfonyl fluoride (PMSF), 8 M urea, 5% w/v sodium dodecyl sulfate (SDS), and the complete protease inhibitor cocktail (Roche Diagnostics GmbH, Mannheim, Germany)]. After the addition of glass beads (0.5 mm), cells were disrupted by seven cycles of vigorous vortexing (1 min) and cooling on ice (1 min) with a Multi-beads shocker (Yasui Kikai, Osaka, Japan). Samples were centrifuged at 5,000 *g* for 10 min at 4°C to remove unbroken cells and cell walls.

Immunoblot Analysis

Proteins from the yeast whole-cell extract were separated by electrophoresis on a 12% SDS polyacrylamide gel and electrotransferred onto a BioTrace NT nitrocellulose membrane (Pall Corp., Port Washington, NY). The membrane was blocked with 5% (w/v) non-fat dried milk in PBS-T buffer [pH 7.5; 80 mM Na_2HPO_4, 20 mM NaH_2PO_4, 100 mM NaCl, and 0.05% (v/v) Tween20]. Membranes were stained overnight at 4°C with a horseradish peroxidase (HRP)-conjugated rabbit anti-c-myc polyclonal antibody (GE Healthcare UK Ltd., Buckinghamshire, England) in the PBS-T buffer containing 5% non-fat dried milk. After washing, the blots were developed using an enhanced chemiluminescence (ECL) detection kit (Millipore, Billerica, MA).

Immunodetection and Fluorescence Microscopy

The yeast cells were fixed in 3 mL of ice-cold methanol for 8 min at −80°C, added to PEM buffer [pH 6.9; 100 mM piperazine-1,4-*bis*(2-ethanesulfonic acid) (PIPES), 1 mM ethylene glycol tetraacetic acid (EGTA), and 1 mM $MgCl_2$], harvested and washed twice with additional PEM buffer. Cells were then resuspended in PEMS buffer [PEM buffer containing 20% (v/v) sorbitol)] with 0.1 mg/mL zymolyase-100T (Seikagaku Biobusiness Corp., Tokyo, Japan) and incubated at 37°C for 1 h. The spheroplasts were harvested, resuspended in PEM buffer containing 1% (v/v) bovine serum albumin (BSA) and incubated at room temperature for 30 min. Then, they were stained overnight with a fluorescein isothiocyanate (FITC)-conjugated anti-c-myc polyclonal antibody (1:50) in the PEM-BSA buffer. Immunolabeled spheroplasts were observed with a Zeiss Axio Imager M1 fluorescence microscope (Carl Zeiss, Jena, Germany).

The *luc* Reporter Gene Assay for OR Function in Yeast

Induced cells were transferred into fresh SGR media and cultivated until the early stage of exponential growth phase was reached (D_{600} in the range 0.4–0.5). Then DNT (Wako Pure Chemical Industries, Ltd., Osaka, Japan) that had been dissolved in dimethyl sulfoxide prior to use was added. The cells were then incubated until the late stage of exponential growth phase was reached (D_{600} in the range 1.0–1.2). For the *luc* reporter gene assay, 100 μL of cell culture was mixed with an equal volume of citrate buffer [pH 3.0; 93 mM citrate and 7 mM sodium citrate] containing 1 mM D-luciferin potassium (Wako Pure Chemical Industries, Ltd.). The generated bioluminescence was measured with a PMT plate reader (Hamamatsu photonics, Shizuoka, Japan) (detection range: 300–650 nm, detection time: 10 s).

Results and Discussion

A General Strategy for Odorant Sensing in Yeast

Radhika et al. constructed a cAMP-responsive olfactory detection system by introducing genes to express the rat heterotrimeric G protein $G\alpha_{olf}$, which is specifically expressed in olfactory neuron cells with ORs, $G\beta_2$, $G\gamma_5$, the olfactory epithelium-specific adenylyl cyclase (type III adenylyl cyclase or ACIII), the human cAMP response element binding protein (CREBP), and the cAMP response element (CRE)-driven *GFP* reporter (Radhika et al., 2007). Although this system is very elegant, we chose a more simple strategy that made use of the endogenous G-protein signaling pathway that serves as the mating machinery in yeast cells (Ishii et al., 2008).

S. cerevisiae inherently possess an uncompetitive and monopolistic G protein signaling pathway (pheromone signaling pathway; Iguchi et al., 2010; Togawa et al., 2010). Binding of the α-factor pheromone to the endogenous GPCR Ste2 activates the heterotrimetric G-protein that consists of the Gpa1 (Gα), Ste4 (Gβ), and Ste18 (Gγ) subunits. Upon activation, a signal is transduced inside the cells and causes global changes in transcription (Ishii et al., 2008). One of the genes that are activated by this process, *FUS1*, is commonly used as a reporter gene for monitoring changes in GPCR signaling (Ladds et al., 2005; Minic et al., 2005b). Therefore, the replacement of *FUS1* by a reporter gene, such as *luc*, enables us to detect the signal transmitted from the GPCRs (Minic et al., 2005a). If the OR is functionally expressed on the yeast cell surface in place of the Ste2 receptor, the engineered yeast cell activates intracellular signaling through the coupling of the OR and Gpa1 in response to an odor molecule. Thus, this system would permit the use of yeast as highly sensitive odor sensors. Additionally, the substitution of Gpa1 with G_{olf} could ensure a more efficient coupling of the OR with the corresponding G-protein subunit to enhance intracellular signaling (Radhika et al., 2007).

Thus, we decided to construct an odor sensor using the highly sensitive *luc* reporter gene controlled by the *FUS1* promoter to examine the effects of replacing the N-terminus in the chimeric receptor on the functional expression of ORs.

The Construction and Expression of Chimeric ORs in *S. cerevisiae*

To investigate the roles of the N-terminal region of the ORs on their functional expression in yeast, we constructed the following three types of chimeric mOR226 genes: (i) mOR226 with only the C-terminal replaced by 33 corresponding aa residues of RI7 (N_{intact}OR226), (ii) mOR226 with the C-terminal replacement in N_{intact}OR226 in combination with the replacement of the N-terminal with 32 corresponding aa residues of RI7 ($cI7_{N32}$OR226) and 3) mOR226 with the C-terminal replacement in N_{intact}OR226 in combination with the replacement of the N-terminal with 58 corresponding aa residues of RI7 ($cI7_{N58}$OR22) (Fig. 1). These chimeric cDNAs were inserted downstream of the *GAL1* promoter in the yeast expression vector pESC-URA to fuse the c-myc tag to the N-termini of each chimera (Table I). The *FUS1*-controlled *luc* reporter gene plasmid in combination with each chimeric OR expression vector were introduced into an IM-50 yeast strain with a deletion of the endogenous *STE2* gene to produce the engineered yeast cells for odor sensing utilizing the endogenous GPCR signal transduction system (Table I).

Transcription of the constructed chimeric ORs was detected by RT-PCR using total RNA extracted from the yeast transformants. The bands corresponding to the reverse-transcribed mRNA of the chimeric ORs were present at the expected sizes for all transformants induced in the galactose media (Fig. 2A). Subsequently, a western blot for the c-myc epitope tag added to the N-terminus of the chimeric ORs demonstrated the successful expression of each receptor in the yeast cells (Fig. 2B). The intensities of the bands were different among the three types of receptors with N_{intact}OR226 more abundantly expressed than the other OR chimeras. This result suggests that the replacement of the N-terminus of mOR226 with the corresponding region of RI7 decreased the expression level of chimeric mOR226 in the whole-cell fractions.

Localization of the RI7/mOR226 Chimeric Receptors

To examine the localization of the chimeric ORs on the surface of the yeast cell membrane, yeast spheroplasts were stained with an anti c-myc antibody conjugated to FITC. Aside from the control strain, all transformants exhibited green fluorescence, which demonstrated that all of the chimeric receptors were displayed on the cell surface membranes (Fig. 3). Because the c-myc epitope tag was attached to the N-terminus of the chimeric ORs and the antibody was impermeable to the cell membrane, the fluorescence intensity should reflect the relative number of receptors of the cell surface with N-termini oriented toward

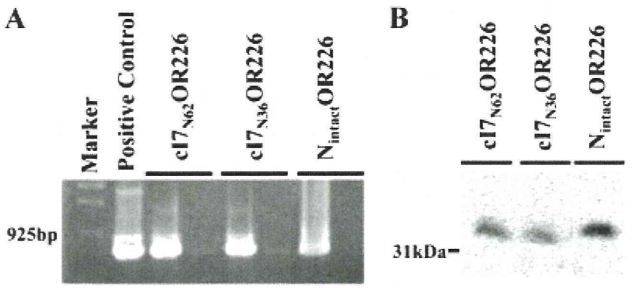

Figure 2. Expression of the RI7/mOR226 chimeric receptors in yeast cells. Transformants expressing FL50-N_{intact}OR226, FL50-$cI7_{N32}$OR226, or FL50-$cI7_{N58}$OR226 were used for the following analyses. **A**: Agarose gel electrophoresis of the RT-PCR products amplified using OR226 specific primers. The marker is λ DNA digested with *Eco*T14I. The positive control is a PCR product amplified from the pESCu-$cI7_{N58}$OR226 vector. The left lanes show PCR products amplified from cDNA created from RT-PCR templates. The right lanes show PCR products amplified from DNase-treated extracts from each transformed cell line to verify the absence of any remaining DNA. **B**: An immunoblot analysis of the RI7/mOR226 chimeric receptors in yeast whole-cell extracts. A HRP-conjugated anti-c-myc antibody was used for the detection of the chimeric proteins.

the outside of the cell membranes. While the chimeric mOR226 with an intact N-terminus (N_{intact}OR226) was widely expressed on the yeast cell membranes, the chimeras with N-terminal replacements ($cI7_{N32}$OR226 and $cI7_{N58}$OR226) appeared to be more abundantly expressed on the cell surface in the correct orientation. This phenomenon was more prominent for $cI7_{N58}$OR226 with the longer N-terminal replacement (Fig. 3). These results support the idea that the replacement of N-terminal region of mOR226 by the corresponding region of RI7 altered the transport pattern of the ORs onto the yeast cell membranes. This alteration may be due to differences in the positions of potential N-glycosylation sites (Asn in the 13th position, NXT of mOR226, and Asn in the 5th position, NXS of RI7) or in the sequences themselves (Fig. 1). In addition, the helix structure of the TM region derived from RI7 might accelerate the transportation or the expression of the chimeric ORs by stabilizing their conformation.

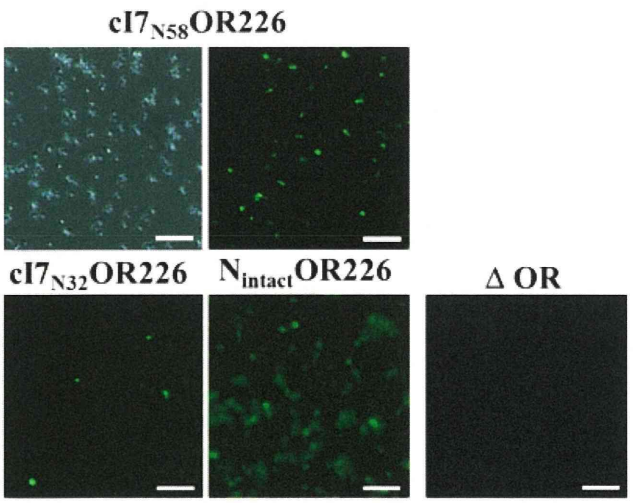

Figure 3. Immunofluorescence of the RI7/mOR226 chimeric receptors in yeast cells. The upper panels show optical (left panel) and fluorescent (right panel) microscopy images of spheroplasts from yeast expressing FL50-$cI7_{N58}$OR226 ($cI7_{N58}$OR226). The lower panels show fluorescent microscopy images of spheroplasts from the FL50-$cI7_{N32}$OR226 ($cI7_{N32}$OR226) or FL50-N_{intact}OR226 (N_{intact}OR226) yeast transformants. FL50-ΔOR (ΔOR) is the negative control yeast strain, which contained the pESC-URA expression vector. Immunolabeling was performed with a FITC-conjugated anti-c-myc antibody to stain for the c-myc epitope tag attached to the N-termini of the chimeric receptors. Scale bar, 10 μm.

DNT Odor-Sensing Capabilities of the RI7/mOR226 Chimeric Receptors Using Yeast Signal Transduction Machinery

To evaluate whether the constructed chimeric ORs were functional on the yeast cell membranes, we tested the odor-sensing abilities of the yeast toward the DNT ligand. The cells were incubated in media containing various concentrations of DNT, and the resulting expression levels of the *luc* reporter gene were measured by bioluminescence.

All transformants exhibited an enhancement of bioluminescence with increasing concentrations of DNT, which indicated that the chimeric ORs were functionally expressed and could bind to the endogenous yeast Gpa1 protein to facilitate signal transduction (Fig. 4). After DNT treatment, $cI7_{N58}$OR226 exhibited the highest luminescence intensities, which suggested that the replacement of the N-terminal region of mOR226 up to the ICL1 domain is more suitable for the functional expression of the RI7/mOR226 chimeric receptor in yeast. This result is consistent with our immunofluorescence staining results (Fig. 3). Thus, the method for replacing the N-terminal region of target ORs by

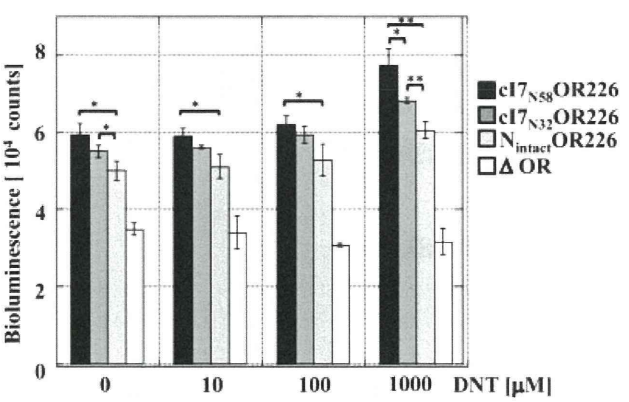

Figure 4. DNT sensing using the *luc* reporter gene assay in yeast cells expressing the RI7/mOR226 chimeric receptors. FL50-N_{intact}OR226, FL50-$cI7_{N32}$OR226, FL50-$cI7_{N58}$OR226, and FL50-ΔOR yeast transformants were tested for their ability to sense the odorant DNT. Bioluminescence was measured in the yeast strains stimulated by addition of DNT in the exponential growth phase in SGR media. The data shown represent the mean ± SEM of three separate experiments. Statistical significance was assessed by the *t*-test ($^{*}P < 0.05$; $^{**}P < 0.01$).